

## REVIEW

[View Article Online](#)  
[View Journal](#) | [View Issue](#)Cite this: *Sustainable Energy Fuels*,  
2020, 4, 5916Received 2nd September 2020  
Accepted 25th September 2020

DOI: 10.1039/d0se01305f

[rsc.li/sustainable-energy](http://rsc.li/sustainable-energy)

## The role of oxygen vacancies in water splitting photoanodes

Roser Fernández-Climent, Sixto Giménez\* and Miguel García-Tecedor \*

Photoelectrochemical water splitting has become one of the most reliable solar-energy conversion technologies for clean hydrogen production. In the race of developing and understanding new semiconducting materials for this application, several studies have been focused on the role of oxygen vacancies, which are known to be defects with a high impact on the final optical and electrical properties of the photoelectrodes. These oxygen defective states can introduce either favorable or detrimental pathways to the overall PEC performance. The present topical review aims to summarize the role of oxygen vacancies in four of the most studied semiconducting thin film oxides ( $\text{BiVO}_4$ ,  $\text{Fe}_2\text{O}_3$ ,  $\text{TiO}_2$  and  $\text{WO}_3$ ) as photoanodes for solar water splitting.

## Introduction

In the current and worrying global environmental situation, light-driven water splitting stands out as one of the most promising alternatives to the obsolete fossil-fuel-based economy for the production of clean energy sources such as hydrogen.<sup>1,2</sup> The required materials for solar water splitting are semiconductors, with a certain bandgap, which can generate an electrical current under illumination. Narrow bandgap semiconductors (ideally  $E_g \sim 2$  eV) are more suitable for solar energy conversion due to their higher optical absorption from the solar spectrum, since all the photons with energies higher than the bandgap can be absorbed. Specifically, n-type semiconductors are required for the Oxygen Evolution Reaction (OER) in order to oxidize water ( $2\text{H}_2\text{O} \rightarrow \text{O}_2 + 4\text{H}^+ + 4\text{e}^-$ ) with the photo-generated holes from the valence band (VB) under illumination conditions. Among the most studied materials for the OER, n-type metal oxide semiconductors such as  $\text{BiVO}_4$ ,<sup>3,4</sup>  $\text{Fe}_2\text{O}_3$ ,<sup>5,6</sup>  $\text{TiO}_2$  (ref. 7 and 8) and  $\text{WO}_3$  (ref. 9 and 10) stand out due to their promising properties. Furthermore, other promising systems such as  $\text{TaON}$ ,<sup>11,12</sup>  $\text{CN}$ ,<sup>13</sup> *etc.* have also been reported. Usually, a thin film, around few hundreds of nm, of the active material is deposited onto a transparent oxide conducting layer (back contact, usually FTO or ITO) with a thickness high enough to present a high optical absorption but lower than the carrier diffusion length to allow efficient charge extraction.<sup>14,15</sup> Specifically, a given semiconductor must have a thickness of  $3/\alpha$ , being  $\alpha$  the absorption coefficient, in order to absorb 95% of the light at that wavelength, as derived from the Beer–Lambert law.<sup>16</sup>

Oxygen vacancies (OVs) constitute one of the most studied defects in oxide semiconductors. These defects, usually intrinsic, are generated by the removal of an oxygen atom from the crystalline structure, which remains charged with two extra electrons.<sup>17,18</sup> Oxygen vacancies could be formed by different mechanisms, including: (i) the formation during the growth of a crystal, (ii) the formation to compensate for the charge introduced by a dopant (ionic compensation), or (iii) pre-existing OVs which diffuse and gather at the interfaces, leading to the formation of an interlayer of a different crystal phase due to their influence on the phase stability.<sup>19</sup> Oxygen vacancies are the most common defects in metal oxides. Due to this fact, any treatment altering the chemical environment (temperature annealing, treatments under different atmospheres during the growth, laser irradiation, *etc.*) of the metal oxide will lead to the formation of these oxygen defective states. However, there is a maximum concentration of OVs where the phase stability of the crystal lattice could be compromised.<sup>20</sup> Oxygen vacancies are responsible in many cases for the exotic electrical and optical properties of different oxide semiconductors.<sup>21–23</sup> Additionally, in recent years, the possibility to tune the population and energy distribution of these defects, through different physical and chemical treatments or doping processes, for specific goals has been extensively exploited.<sup>24–27</sup> However, the detection of structural defects in condensed matter physics has always been a challenge due to their diluted and elusive nature. Several efforts have been undertaken to find suitable strategies to address this issue. Currently, there is a wide range of available techniques, some of them indirect,<sup>28</sup> for the detection of OVs,<sup>29</sup> based on different energy sources such as: (i) electrons, (ii) X-rays or (iii) photons. (i) Among the detection techniques using electrons as the energy source, the most relevant ones are: High-Resolution Transmission Electron Microscopy (HRTEM), corrected by spherical aberration, which

*Institute of Advanced Materials (INAM), Universitat Jaume I, Avenida de Vicent Sos Baynat, s/n, 12006 Castelló de la Plana, Castellón, Spain. E-mail: [sjulia@uji.es](mailto:sjulia@uji.es); [tecedor@uji.es](mailto:tecedor@uji.es)*



can lead to the direct visualization of OVs,<sup>30</sup> Scanning Tunneling Microscopy (STM)<sup>31</sup> and Cathodoluminescence (CL).<sup>32</sup> (ii) X-ray based tools include X-ray Photoelectron Spectroscopy (XPS),<sup>33</sup> X-ray Absorption Spectroscopy (XAS)<sup>34</sup> and X-ray Diffraction (XRD).<sup>25</sup> (iii) Using photons as the energy source, the most usual techniques are Photoluminescence (PL),<sup>35</sup> Raman Spectroscopy,<sup>36</sup> and Fourier Transform Infrared Spectroscopy (FTIR).<sup>37</sup> In the specific case of solar water splitting, the effect of oxygen vacancies on the performance of different photoanodes has been widely reported in different systems.<sup>25,38–40</sup> Oxygen vacancies can act as doping elements introducing defect levels inside the bandgap of the semiconductor, and thus, modifying the different pathways for the electronic processes such as recombination, charge extraction and injection.<sup>41</sup> Specifically, OVs can induce favorable effects on the overall PEC performance by increasing the carrier concentration, being responsible in many cases for the intrinsic n-type conductivity,<sup>42</sup> which favors the formation of a space-charge layer trough doping,<sup>43</sup> or enhancing light absorption,<sup>44</sup> but can also induce detrimental effects such as activation of recombination channels, acting as charge-carrier traps or recombination centers.<sup>45,46</sup>

The present review aims to summarize the main contributions about the role of oxygen vacancies in four of the most studied semiconducting metal oxides as photoanodes for the OER ( $\text{BiVO}_4$ ,  $\text{Fe}_2\text{O}_3$ ,  $\text{TiO}_2$  and  $\text{WO}_3$ ).

### Bismuth vanadate, $\text{BiVO}_4$

During the last few years,  $\text{BiVO}_4$  has emerged as one of the most promising candidates to fabricate reliable photoanodes for photoelectrochemical (PEC) solar water splitting.  $\text{BiVO}_4$  presents three possible phases: tetragonal scheelite, tetragonal zircon and monoclinic scheelite.<sup>47</sup> Among these structures, the monoclinic scheelite structure (Fig. 1), showing a layered nature and belonging to the  $C2/c$  spatial group, is the most active for PEC applications.<sup>48</sup>  $\text{BiVO}_4$  is an n-type semiconductor, with a 2.4 eV bandgap and consequently a theoretical solar to hydrogen (STH) efficiency of 9.2% with a maximum photocurrent of  $7.5 \text{ mA cm}^{-2}$  under AM 1.5 G illumination, low overpotential and favorable band-edge positions.<sup>49</sup> However,  $\text{BiVO}_4$  also presents poor electron transport, high surface recombination and slow water oxidation kinetics. Enormous efforts have

been made in the past few years in order to mitigate these drawbacks through different approaches such as nanostructuring,<sup>50,51</sup> doping,<sup>52,53</sup> heterostructuring<sup>4,54</sup> and the use of efficient co-catalysts.<sup>55,56</sup>

An additional strategy to improve the performance of  $\text{BiVO}_4$  photoanodes relies on the intentional creation of oxygen vacancies.<sup>57,58</sup> Oxygen vacancies in  $\text{BiVO}_4$ , usually associated with  $\text{V}^{4+}$  species, are structural defects, which can introduce shallow levels inside the bandgap. These shallow levels can have favorable effects on the final performance, reducing the recombination processes between photo-generated carriers, and thus, increasing the overall PEC activity. Alternatively, these defects can act as recombination centers and then activate recombination channels, which decrease the final performance. Specifically, the charge separation efficiency can be improved in  $\text{BiVO}_4$  photoanodes by the intentional introduction of a high density of oxygen vacancies, as previously reported.<sup>36,59,60</sup> In these studies, the enhanced performance was systematically correlated with a higher density of oxygen deficiencies, detected mainly by XPS. Frequently, the samples showing a higher density of OVs also showed a higher Incident Photon to Current Efficiency (IPCE), which is a direct measurement of the External Quantum Efficiency (EQE), related to a higher density of extracted photogenerated carriers for the same light irradiation, mainly due to a more efficient optical absorption. However, as explained above, there are other studies, where the defect levels inside the bandgap introduced by oxygen vacancies show a detrimental behavior. As an example, a recent study showed the suppression of the formation of oxygen vacancies leading to a higher PEC performance due to an increase of the conductivity as a consequence of the release of bound polarons.<sup>61</sup>

The synthesis of black  $\text{BiVO}_4$  has been reported, as a new black material.<sup>63</sup> Herein, nanosized black  $\text{BiVO}_4$  colloids were prepared by laser irradiation of bulk particles. By using Raman Spectroscopy and XPS, the black color was associated with the presence of a high concentration of oxygen vacancies in the nanostructure after laser radiation. The new black  $\text{BiVO}_4$  showed a clear improvement in the performance as an anode material for Sodium Ion Batteries (SIBs), compared to pristine  $\text{BiVO}_4$ . The enhanced performance was related not only to the decreased particle size of the black  $\text{BiVO}_4$ , but also to the presence of oxygen vacancies, which can alter the electronic structure improving the conductivity.

Additionally, the presence of oxygen vacancies clearly increases the optical absorption in the visible range, which is favorable for photocatalytic applications such as PEC water splitting. However, an excess density of oxygen vacancies could induce a metal-like behavior (degenerated semiconductor), leading to the deactivation of the photoactivity of the material and consequently, decreasing the overall performance towards the OER. Although the application explored in this study is out of the scope of the present review, this work opens a new possibility for the design of black  $\text{BiVO}_4$  as a photoanode for water splitting with enhanced performance towards the OER.

Several theoretical studies have also tried to shed light on the role of oxygen vacancies in  $\text{BiVO}_4$  photoanodes.<sup>64,65</sup> Oxygen vacancies have been found to present two possible geometries

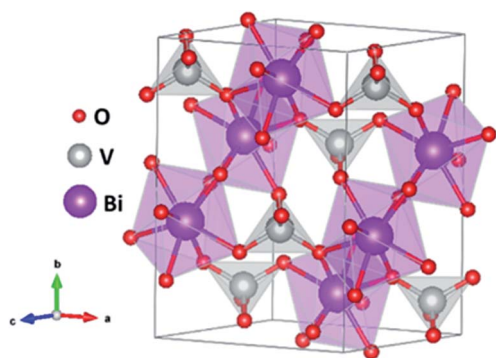


Fig. 1 Monoclinic structure of  $\text{BiVO}_4$  obtained with VESTA software.



of a V–O–V bridge, allowing excess electrons to be delocalized in a two-dimensional charge state or localized in different V centers.<sup>62</sup> These V–O–V bonds present low transition energies, which allow their consecutive formation and destruction, leading to the migration of oxygen vacancies in the bulk of BiVO<sub>4</sub> and increasing both electronic and ionic conductivities.<sup>66,67</sup> Due to the complexity of BiVO<sub>4</sub>, all these possible electronic configurations (Fig. 2) have a direct impact on its final performance towards solar water splitting. Another recent theoretical study reported that the location of oxygen vacancies, in the bulk or at the surface, influences the overall performance of BiVO<sub>4</sub> photoanodes in a completely different direction.<sup>64</sup> Specifically, this study claimed that both oxygen vacancies in the bulk and at the surface introduce donor levels inside the band gap. However, the formation of bulk polarons, due to the migration of electrons associated with oxygen vacancies, contributes to the conductivity while surface polarons likely do not, acting as possible recombination centers.

The occupancy of the electronic states associated with OVs can also be modulated in order to move one step forward in the modification of BiVO<sub>4</sub> photoanodes. In a recent study,<sup>68</sup> the population of the electronic states associated with OVs in BiVO<sub>4</sub> photoanodes were modulated by using several spectroscopic techniques. This study concluded that oxygen vacancies participate in the trapping of photogenerated carriers in addition to their well-known role enhancing the n-doping and the

formation of the space-charge layer. Photogenerated holes are trapped by V<sub>OV</sub><sup>4+</sup> states in the bulk, leading to a loss pathway, since these states are above the water oxidation level and thus are not able to participate in the OER. However, photogenerated electrons are trapped in V<sub>OV</sub><sup>5+</sup> states in the space-charge layer with an activation energy of around 0.2 eV. Thus, these electrons can be extracted with some thermal activation, improving the PEC performance of the BiVO<sub>4</sub> photoanodes. The role of oxygen vacancies in trapping and transport processes of BiVO<sub>4</sub> photoanodes is depicted in the scheme shown in Fig. 3.

A recent study has reported the suppression of OVs in the bulk with the concomitant increase in the generation of these defects at the surface of BiVO<sub>4</sub>, by a photoetching process.<sup>69</sup> This study also claims that the formation of oxygen vacancies at the surface leads to a noticeable improvement in the final PEC activity towards water oxidation due to an increase in the carrier density, enhancing the band-bending, and then improving the charge separation efficiency by a factor 2.3 compared to pristine BiVO<sub>4</sub>.

An additional approach to improve the performance of BiVO<sub>4</sub> photoanodes consists of the deposition of a certain electrocatalyst with a high concentration of oxygen vacancies. It has been already reported that oxygen vacancies lead to an increase of the density of catalytic sites improving then the overall performance of the BiVO<sub>4</sub>-catalyst system.<sup>70</sup> The same strategy was followed to improve the PEC activity of  $\alpha$ -Fe<sub>2</sub>O<sub>3</sub> photoanodes with a high oxygen-defective CoO<sub>x</sub> electrocatalytic layer.<sup>71</sup> However, this approach is out of the scope of this review.

### Hematite, Fe<sub>2</sub>O<sub>3</sub>

Hematite has been widely studied as a solar water splitting photoanode due its abundance, low-cost, non-toxicity, and favorable physical properties, such as its narrow bandgap (2.1 eV) and high chemical stability.<sup>5,72–74</sup> Fe<sub>2</sub>O<sub>3</sub> has a theoretical maximum photocurrent of 12.6 mA cm<sup>−2</sup>, which corresponds to a STH efficiency of 16.8%.<sup>75</sup> Among the different existing phases,  $\alpha$ -Fe<sub>2</sub>O<sub>3</sub>, with an orthorhombic–trigonal structure (Fig. 4) belonging to the R3c spatial group, is the most active phase for solar water splitting. Nevertheless, hematite also shows severe limiting factors as poor electrical conductivity, a short hole diffusion length (2–4 nm),<sup>76</sup> poor OER kinetics,<sup>77</sup> and non-favorable band positions for water splitting.<sup>78</sup> Several approaches have been reported to overcome these drawbacks,

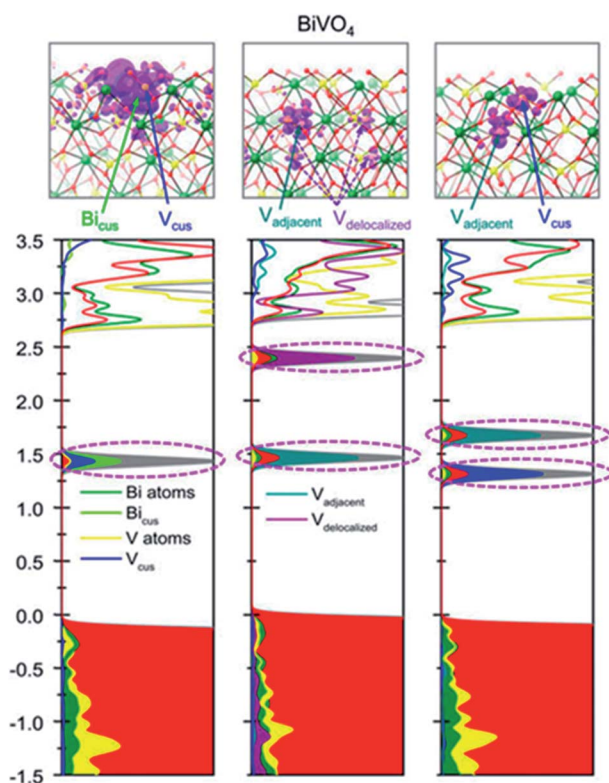


Fig. 2 Intra-gap states introduced by the different electronic configurations associated with oxygen vacancies in BiVO<sub>4</sub>. This figure has been reproduced from ref. 62 with permission from AIP, copyright 2020.

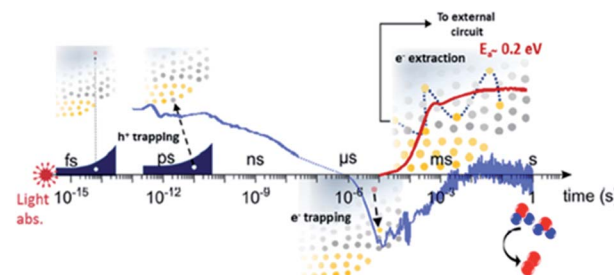


Fig. 3 Scheme of the role of oxygen vacancies in trapping and transport processes in BiVO<sub>4</sub> photoanodes. This figure has been reproduced from ref. 68 with permission from ACS, copyright 2019.





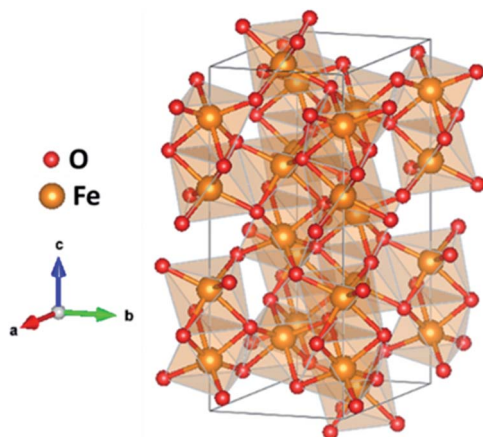
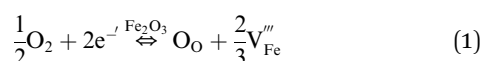


Fig. 4 Orthorhombic-trigonal structure of  $\text{Fe}_2\text{O}_3$  obtained with VESTA software.

such as extrinsic doping,<sup>79,80</sup> nanostructuring,<sup>81</sup> the use of electrocatalysts<sup>82,83</sup> and complex architectures.<sup>84</sup> An additional possibility consists of the intrinsic doping of hematite photoanodes with oxygen vacancies. The role of these defects in  $\alpha\text{-Fe}_2\text{O}_3$  photoanodes for solar water oxidation has been extensively reported as a beneficial factor to their final performance.

Several studies reported fabrication methods to tune the concentration of oxygen vacancies for improved PEC performance: Li *et al.*<sup>85</sup> reported a fabrication method of  $\alpha\text{-Fe}_2\text{O}_3$  photoanodes through thermal decomposition of  $\beta\text{-FeOOH}$  in an  $\text{N}_2$ -rich atmosphere. The resulting hematite showed enhanced photoactivity due to an increase in the electrical conductivity through a polaron hopping mechanism<sup>86</sup> as a result of the formation of oxygen vacancies, and thereby  $\text{Fe}^{2+}$  sites. Other studies combined the generation of oxygen vacancies with extrinsic doping (with Ti, Sn, *etc.*) to improve the activity<sup>25</sup> by increasing the electrical conductivity. Specifically, Sun *et al.*<sup>87</sup> claimed that oxygen vacancies increase the donor density with a lower oxidation state of iron ( $\text{Fe}^{2+}$ ), while Ti-doping improves the catalytic response by the introduction of active sites, increasing the final performance of the fabricated photoanodes. The final activity of hematite photoanodes can also be tuned through thermal annealing in different environments.<sup>88</sup> In this study, the effect of thermal annealing under different atmosphere on Nb- and Si-doped  $\text{Fe}_2\text{O}_3$  photoanodes was analyzed. When the samples were annealed in air, oxygen can be incorporated as  $\text{O}^{2-}$  in the hematite lattice ( $\text{O}_\text{O}$ ). This excess oxygen is then compensated for by the creation of cation vacancies ( $\text{V}_{\text{Fe}}'''$ ) following the equation:



These cation vacancies are surrounded by anions and act as critical recombination centers for holes, decreasing the photocurrent. On the other hand, annealing under an oxygen-free atmosphere (Ar) leads to the formation of oxygen vacancies, due to the reduced oxygen partial pressure, increasing the carrier concentration present in the photoanodes and thus, the

photocurrent. In the same direction, a recent study reported the enhanced performance of  $\text{Fe}_2\text{O}_3$  photoanodes after thermal annealing in a low oxygen atmosphere, showing that oxygen vacancies improved the transport of photogenerated holes.<sup>89</sup>

Theoretical Density Functional Theory (DFT) studies have also been focused on the effect of oxygen vacancies on the overpotential and final performance of  $\text{Fe}_2\text{O}_3$  photoanodes. It has been reported that the most efficient way to reduce the overpotential in hematite photoanodes relies on the control of the population of oxygen vacancies.<sup>90</sup> Specifically, the authors calculated an overpotential as low as 470 mV for an optimal concentration of oxygen vacancies of 12.6 vacancies per  $\text{nm}^2$ , which is one of the lowest densities among theoretical studies,<sup>91,92</sup> as shown in Fig. 5. The enhanced performance of hematite photoanodes after  $\text{N}_2$  treatments has also been reported.<sup>93</sup> The experimental results showed that the enhanced performance induced by the presence of OV was related to an increase of both charge separation and charge transfer efficiencies. Combining these experimental results with DFT calculations, it was found that the enhanced charge separation was achieved by the increased electron density combined with a decrease in the surface potential which improves the hole transport from the bulk to the (110) surface. Additionally, oxygen vacancies expose Fe atoms on the surface leading to an increase of the population of active sites.

A recent study has reported the effect of the location of oxygen vacancies on the final behavior of the  $\text{Fe}_2\text{O}_3$  photoanode.<sup>94</sup> Bulk oxygen vacancies were reported to have a negative impact on the performance of the hematite photoanodes for water oxidation. However, the surface oxygen vacancies were able to narrow the space charge region width, boosting the charge separation and charge transport of the photoanodes (Fig. 6a and b). Additionally, the water adsorption and hydrophilicity of  $\alpha\text{-Fe}_2\text{O}_3$  were modified by the surface oxygen vacancies, improving the kinetics of water oxidation.

### Titanium dioxide, $\text{TiO}_2$

Since the pioneering study of Fujishima and Honda in 1972,<sup>95</sup> many researchers focused their studies on  $\text{TiO}_2$  materials for

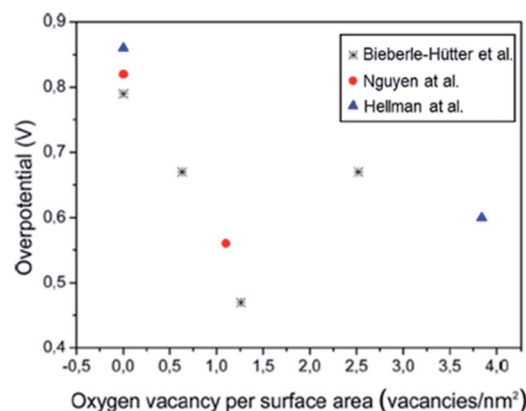


Fig. 5 Calculated overpotentials as a function of the concentration of oxygen vacancies. This figure has been reproduced from ref. 90 with permission from ACS, copyright 2016.



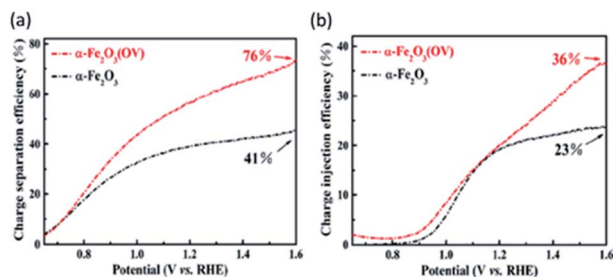


Fig. 6 (a) Charge separation ( $\eta_{\text{sep}}$ ) and (b) charge injection ( $\eta_{\text{cat}}$ ) efficiencies of pristine and oxygen vacancy-rich  $\alpha\text{-Fe}_2\text{O}_3$  (OV) photoanodes. This figure has been reproduced from ref. 94 with permission from ACS, copyright 2020.

photocatalytic applications due to its earth abundance, low cost, chemical and thermal stability, high refractive index, non-toxicity, and high photocatalytic activity under adequate radiation.<sup>96–98</sup> Specifically,  $\text{TiO}_2$  is an n-type semiconductor with three different polymorphs: rutile ( $E_g = 3.0$  eV), anatase ( $E_g = 3.2$  eV), and brookite ( $E_g = 1.9$  eV), rutile being thermodynamically stable whereas the other two phases are metastable.<sup>99,100</sup> Rutile and anatase have been the most studied phases, anatase (Fig. 7) being the most efficient one for photocatalytic applications due to the lower charge carrier recombination and higher surface adsorption for hydroxyl groups.<sup>101</sup> Despite all the positive properties mentioned above, the large bandgap of anatase and rutile  $\text{TiO}_2$  limits their optical absorption to ultraviolet (UV) light, leading to the efficient utilization of only a small part of the solar spectrum ( $\sim 5\%$ ), giving a theoretical maximum photocurrent of  $1.1 \text{ mA cm}^{-2}$  and a STH efficiency of 1.3% for anatase and  $1.8 \text{ mA cm}^{-2}$  and 2.2% STH for rutile.<sup>49</sup> Moreover, due to its wide bandgap,  $\text{TiO}_2$  also suffers from rapid electron-hole recombination, which decreases its overall conversion efficiency.<sup>102,103</sup> Different groups tried to overcome the aforementioned limitations to enhance the photocatalytic performance by extending the absorption edge of the solar spectrum to the visible region. Some strategies have been proposed to enhance the light harvesting efficiency based on bandgap

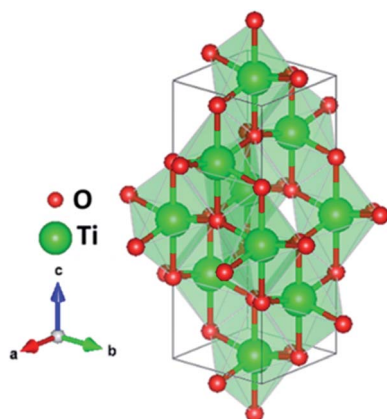


Fig. 7 Crystalline structure of the tetragonal anatase  $\text{TiO}_2$ , belonging to the spatial group  $I4_1/amd$ , obtained with VESTA software.

engineering of  $\text{TiO}_2$  by dye<sup>104</sup> or quantum dot sensitization,<sup>105</sup> doping with N, C, and S atoms<sup>7,106–108</sup> or heterostructuring.<sup>109–111</sup>

However, the most efficient and widely employed strategy for enhancing the photocatalytic activity of  $\text{TiO}_2$  photoanodes is by tuning the density of OV and  $\text{Ti}^{3+}$  interstitials, which are the dominant intrinsic defects in this material.<sup>112–115</sup> Several studies have demonstrated that OV and  $\text{Ti}^{3+}$  play a critical role in determining the surface and electric properties of  $\text{TiO}_2$  since they are capable of creating localized mid gap states.  $\text{Ti}^{3+}$  surface defects are generated by the reduction of  $\text{Ti}^{4+}$  ions due to the loss of oxygen atoms in a reductive treatment or due to electron trapping under UV radiation.<sup>24,112,116</sup> The presence of OV in  $\text{TiO}_2$  could increase the donor density and effectively promote the separation and transport of photogenerated electron-hole pairs.<sup>117,118</sup> OV are easily induced by the reduction of  $\text{TiO}_2$  ( $\text{TiO}_{2-x}$ ). Many synthetic routes have been reported to reduce  $\text{TiO}_2$ , such as metal reduction,<sup>119</sup> ionothermal processes,<sup>120</sup>  $\text{NaBH}_4$  reduction,<sup>121</sup> vacuum annealing<sup>122,123</sup> and hydrogenation.<sup>124</sup>

The synthesis of OV-rich  $\text{TiO}_2$  resulted in a black material with enhanced solar light harvesting and photocatalytic performance. Although in 2001 Lu *et al.*<sup>125</sup> firstly reported an opaque black color of  $\text{TiO}_2$  after a reducing treatment due to some induced defects, the term “Black  $\text{TiO}_2$ ” did not appear until 2011, when Chen *et al.*<sup>126</sup> synthesized black  $\text{TiO}_2$  by introducing surface disorder into the  $\text{TiO}_2$  nanocrystals through a hydrogenation process. The term “Black” was employed due to the visual aspect of this material, in contrast to the usual whitish color of pristine  $\text{TiO}_2$ . Such a significant enhancement in the photocatalytic performance of black  $\text{TiO}_2$  photoanodes is due to the presence of OV and/or  $\text{Ti}^{3+}$  defects. The electron transition from the valence band (VB) to the OV mid-levels and/or from the OV to the VB results in visible and infrared light absorption. This  $\text{TiO}_2$  material with a high concentration of structural defects showed a higher performance towards water oxidation under full illumination (all over the solar electromagnetic spectrum), as shown in Fig. 8a.<sup>119</sup> However, photogenerated holes from the energy levels of OV cannot contribute to PEC performance because they are located above the  $\text{H}_2\text{O}/\text{O}_2$  oxidation potential, and consequently did not contribute to enhance the PEC performance of black  $\text{TiO}_2$  under visible light illumination (Fig. 8b), although these oxygen defective states

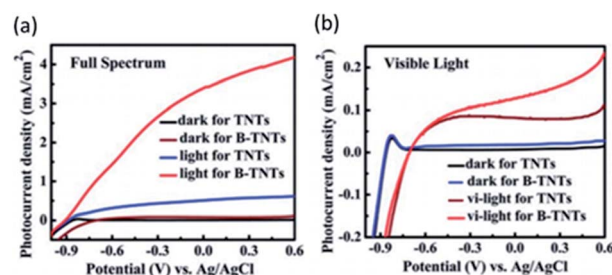


Fig. 8 Current density for pristine  $\text{TiO}_2$  nanotubes (TNTs) and black  $\text{TiO}_2$  nanotubes (B-TNTs) in the dark and under solar illumination of the (a) full spectrum or only (b) visible light. This figure has been reproduced from ref. 119 with permission from RSC, copyright 2014.

can oxidize other scavengers<sup>127</sup> and reduce recombination.<sup>128</sup> The enhanced PEC activity of black TiO<sub>2</sub> under full solar light could be mainly ascribed to the enhanced charge transport and charge separation together with visible light photoresponse.<sup>129</sup>

Some studies reveal an anodic shift of the VB position of TiO<sub>2</sub> due to the presence of OV<sub>s</sub><sup>119,130</sup> that could be followed by a band tail<sup>121</sup> resulting in a narrowed band gap which extends its optical absorption to the visible region, as shown in Fig. 9a. In a recent study, vacuum annealing and Zr doping were explored to improve the performance of nanostructured TiO<sub>2</sub> photoanodes.<sup>123</sup> Both doping and vacuum treatment led to a slightly stressed surface and consequently to a catalytically more active TiO<sub>2</sub> surface, concomitant with the creation of oxygen vacancies, which enhanced carrier transport. Vacuum annealing induced an anodic band shift, thermodynamically beneficial for the accumulation of photogenerated holes needed for water oxidation. Moreover, both Zr doping and vacuum annealing induced optical scattering, enhancing the optical pathway of incoming light and slightly increasing the light harvesting efficiency of the TiO<sub>2</sub> nanostructured films. However, this topic is controversial among the scientific community since other studies reported no displacement in the VB location,<sup>129,131</sup> as shown in Fig. 9b. Maybe these differences could be due to the employed synthetic route, since it has been claimed that hydrogen treatment has a negligible effect on the valence band position at the TiO<sub>2</sub> surface.<sup>118</sup>

Other studies have been focused on modifying the synthetic conditions of black TiO<sub>2</sub> to find an optimum material and simultaneously gaining mechanistic insights into the behavior of defects. Hou *et al.*<sup>131</sup> calcined a TiO<sub>2</sub> sample at different temperatures in air and a vacuum to generate different OV concentrations and studied its photocatalytic performance. The experimental results indicated that samples calcined in air had only bulk OV<sub>s</sub> while those calcined in a vacuum possessed bulk and surface OV<sub>s</sub>. The bulk OV<sub>s</sub> mainly act as recombination centers for the photogenerated charges under total illumination, but extended the light absorption under visible light irradiation. However, surface OV<sub>s</sub> improve the visible light response and capture photogenerated electrons, inhibiting recombination. Then, the visible light photocatalytic performance was noticeably improved under the combined influence of the bulk and surface oxygen vacancies. Park *et al.*<sup>132</sup> extended

the optical absorption to the visible range (300–420 nm) of black TiO<sub>2</sub> photoanodes by introducing a “crystal-deficient” TiO<sub>2</sub> overlayer. In addition, this “crystal-deficient” overlayer induced a 50-fold enhancement of the electrical conductivity, which noticeably increased the electron diffusion length to ~20 μm, ensuring electron collection, since the employed TiO<sub>2</sub> nanostructures were around 2 μm long, leading to enhanced PEC activity.

### Tungsten oxide, WO<sub>3</sub>

WO<sub>3</sub> is a widely studied metal oxide semiconductor for PEC water splitting. Among the different crystalline polymorphs, the monoclinic γ-WO<sub>3</sub>, belonging to the P2<sub>1</sub>/c space group, is the most common phase (Fig. 10).<sup>133</sup> WO<sub>3</sub> is an n-type semiconductor with a bandgap of 2.6 eV and a thermodynamically favorable valence band (VB) position for water oxidation.<sup>134</sup> This semiconducting oxide has a theoretical maximum photocurrent of 3.9 mA cm<sup>-2</sup>, which corresponds to a STH efficiency of 4.8%.<sup>135</sup> Additionally, WO<sub>3</sub> also shows a good photocurrent onset for water oxidation, particularly in an acidic environment.<sup>136</sup> However, WO<sub>3</sub> presents a limited performance towards the OER due to a high electron–hole recombination.<sup>137</sup> Analogous approaches, applied to other water splitting photoanodes to improve their performance, such as extrinsic doping<sup>138</sup> and the use of hetero-architectures<sup>139,140</sup> have also been reported for WO<sub>3</sub>.

Oxygen vacancies are intrinsic dopants which have a highly relevant role in WO<sub>3</sub> photoanodes by introducing donor levels inside the bandgap and being responsible for the n-doping.<sup>141</sup> The formation of OV<sub>s</sub> in WO<sub>3</sub> (in chemical equilibrium) can be expressed as:



where O<sub>O</sub><sup>×</sup> represents the neutral oxygen atom and V<sub>O</sub><sup>×</sup> represents the neutral oxygen vacancy with two trapped electrons, introducing a donor level in the gap. Upon increasing the temperature, the donor levels are successively ionized, with an activation energy *E*<sub>a</sub>, generating free electrons, *e*, in the conduction band. This process can be expressed as:



where V<sub>O</sub><sup>2+</sup> represents a doubly ionized oxygen vacancy. Then, the total equilibrium for carrier generation is given as:

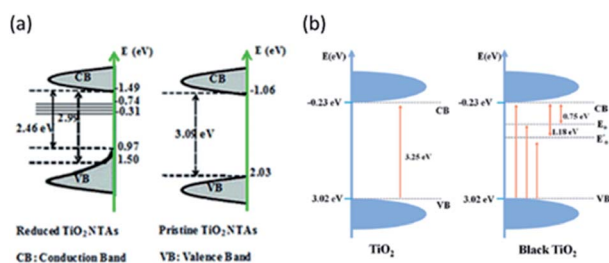


Fig. 9 Energy diagrams for pristine and black TiO<sub>2</sub> (a) with and (b) without VB shift. These figures have been reproduced from ref. 121 and 129 with permission from RSC, copyright 2013 and ACS, copyright 2017, respectively.

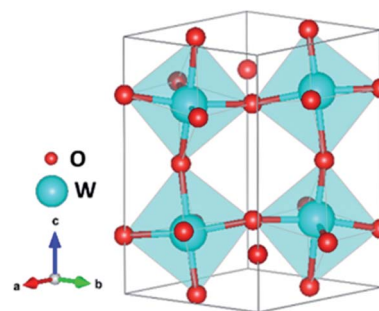
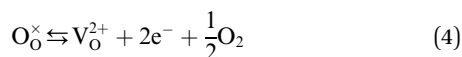


Fig. 10 Monoclinic structure of γ-WO<sub>3</sub> obtained with VESTA software.







The electrical conductivity of  $\text{WO}_3$  has been reported to be a consequence of the carrier generation originating from the formation of oxygen vacancies at the surface.<sup>141</sup> This result was also confirmed by theoretical studies.<sup>142</sup> In this last work, the authors also reported that the localized character of the polaron depended on the concentration of oxygen vacancies in  $\text{WO}_3$  photoanodes. The polaron state was a highly localized state for concentrations of OVs  $\sim 0.8\%$ , whereas it has a 2D character for concentrations of  $\sim 0.4\%$  or smaller. In the case of concentrations of  $\sim 0.1\%$ , the extension of the polaron was calculated to be approximately 1 nm, in agreement with experimental results. This 2D polaron induces a delocalized state at the surface enhancing surface reactivity towards water oxidation intermediates and thus, improving the performance. In good agreement with the latter study, another theoretical study also reported that the excess of charge generated by OVs was partially delocalized at the surface.<sup>143</sup> Additionally, the authors analyzed the interaction between  $\text{H}_2\text{O}$  and  $\text{WO}_3$  on pristine and defective surfaces and reported that OVs did not strongly influence the  $\text{H}_2\text{O}$  adsorption, the process being, in both cases, non-dissociative.

Additionally, the density of oxygen vacancies present in the  $\text{WO}_3$  lattice can be tuned to improve its performance. By combining thermal treatments under a  $\text{H}_2$  atmosphere and the deposition of plasmonic nanoparticles (Au and Ag) on  $\text{WO}_3$  photoanodes, Mathur *et al.*<sup>144</sup> were able to increase the population of OVs, leading to a higher optical absorption (the samples change from transparent to a greyish color), higher stability in acidic environments and an increase in the carrier density and hence, improving the PEC performance. Lately, S.-P. Chai *et al.*<sup>137</sup> tuned the OV concentration by adjusting the concentration of HCl employed during the synthesis. Moreover, it was also observed that a higher amount of this acid leads to a more completed formation of pristine  $\text{WO}_3$ , while a lower amount caused bulk OVs to form instead. The surface oxygen vacancies narrow the bandgap, as observed in other oxide

semiconductors,<sup>145</sup> and downshift both the VB and CB, leading to a better utilization of the solar spectrum and thermodynamically more favorable energetics towards water oxidation, decreasing the overpotential associated with this reaction. Besides, OVs induced sub-band states which improve the charge separation, as schemed in Fig. 11.

However, other groups reported experimental methods to suppress the excessive formation of OVs at the surface, which could enhance the recombination kinetics and thus, reduce the PEC performance.<sup>146</sup> Specifically, an ozone treatment was employed to reoxidize the  $\text{W}^{5+}$  ions on the surface, reducing the concentration of excess OVs and shifting the overpotential cathodically by around 150 mV. There are several studies where the population of oxygen vacancies is optimized to improve the final PEC performance of  $\text{WO}_3$  photoanodes.<sup>147,148</sup> In a very recent study,<sup>149</sup> the performance of  $\text{WO}_3$  photoanodes was analyzed as a function of the concentration of bulk OVs from a kinetic perspective, since apart from all the thermodynamic effects detailed above, such as narrowing the bandgap, introducing defect levels and shifting the VB maximum, oxygen vacancies in  $\text{WO}_3$  photoanodes also induce kinetic effects. In this work, four different concentrations of OVs were studied, “very high” ( $\sim 5.8\%$  oxygen atoms), “high” ( $\sim 2.3\%$  oxygen atoms), “medium” ( $\sim 2\%$  oxygen atoms) and “low” ( $\sim 0.5\%$  oxygen atoms), using transient absorption spectroscopy (TAS) to analyze their impact on the charge carrier recombination kinetics over different time scales, from picoseconds to seconds. The sample with an excess concentration of OVs showed the lowest photocurrent due to high hole trapping kinetics taking place faster than the instrument detection. The sample with a “high” concentration of OVs has a higher bulk trap recombination rate (from hole trapping) limiting the concomitant carrier collection. In the sample with a low concentration of OVs, charge separation is limited, since there are too few defect states, increasing the bimolecular recombination. However, the sample with the balanced concentration of

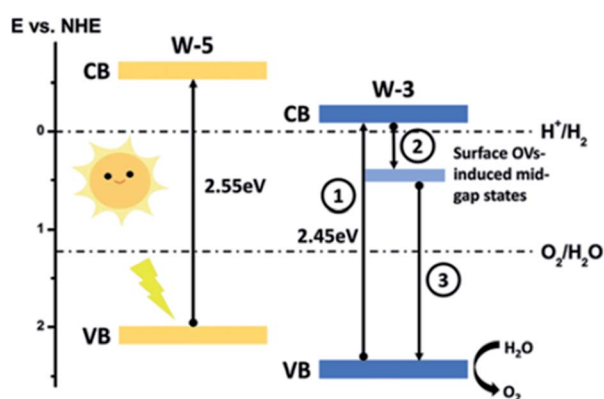


Fig. 11 Energy band diagram of pristine (W-5) and oxygen-vacancies rich (W-3)  $\text{WO}_3$ . This figure has been reproduced from ref. 137 with permission from RSC, copyright 2019.

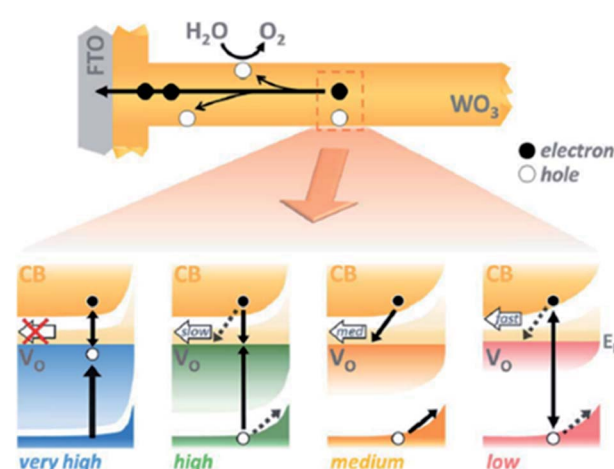


Fig. 12 The role of oxygen vacancies in charge separation and electron transport in  $\text{WO}_3$ , from femtoseconds to seconds. This figure has been reproduced from ref. 149 with permission from RSC, copyright 2020.



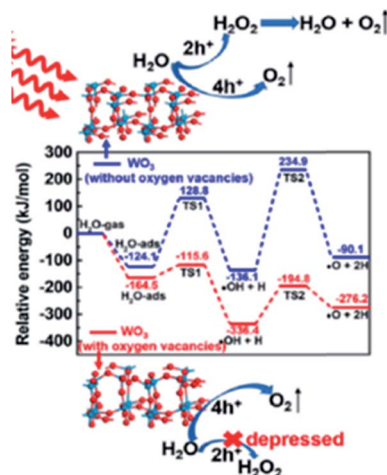


Fig. 13 Potential energy profiles for water dehydrogenation to  $O_2$ . This figure has been reproduced from ref. 150 with permission from ACS, copyright 2019.

OVs delivered the highest photocurrent due to a beneficial equilibrium between charge separation and trap-mediated recombination. The performance of this four different samples is summarized in Fig. 12.

Another kinetically focused study<sup>150</sup> revealed that  $WO_3$  containing oxygen vacancies is more prone to follow the four-hole pathway, instead of the more likely two-hole pathway followed by pristine  $WO_3$ .

This result explained the better performance of  $WO_3$  containing OVs in terms of faster kinetics, higher stability and higher faradaic efficiency towards oxygen compared to stoichiometric  $WO_3$ . The four-hole pathway is schematized in Fig. 13 for both pristine  $WO_3$  and OV-rich  $WO_3$  photoanodes, where the route for the latter is energetically more favorable. In contrast, the oxidation process from  $H_2O$  to  $H_2O_2$ , a two-hole pathway, was found to be energetically more favorable in pristine  $WO_3$ .

## Summary and outlook

The present topical review is focused on the role of oxygen vacancies in four highlighted water splitting photoanode materials,  $BiVO_4$ ,  $Fe_2O_3$ ,  $TiO_2$  and  $WO_3$ . Oxygen vacancies are spontaneously present, as intrinsic dopants, in all these materials inducing their n-type behavior and introducing defect levels at different depths inside the bandgap. The particular location of these oxygen-defective states within the bandgap of the semiconductor leads to different consequences: specifically, surface oxygen vacancies are beneficial for the final performance of water splitting photoanodes, since they improve the charge separation by narrowing the space charge layer. However, in general, bulk oxygen vacancies are detrimental since they enhance recombination dynamics and thus, activate loss channels, with a concomitant decrease of the photocurrent. The concentration of these defects also has a significant effect on the final performance, and the optimization of defect density

is crucial for the development of competitive photoanodes for PEC water splitting. But then, a key question arises: are oxygen vacancies beneficial or detrimental to the final PEC performance of water splitting photoanodes? Most likely, the answer to this question is “depending on the concentration and its location”. Since the presence of these defects, often intrinsic, as well as their concentration and their location within the bandgap, induces severe modifications, the smart tuning of these parameters can lead to significantly enhanced water splitting photoanodes and other solar-related applications. As it has been acutely detailed herein, the population of OVs can be easily tuned by several techniques, leading to a dramatically modified performance towards the OER. Consequently, we believe that the modulation of the population of OVs, and other structural defects, will be greatly exploited in the race for improving solar water splitting photoanodes in the near future.

## Conflicts of interest

There are no conflicts to declare.

## Acknowledgements

We acknowledge financial support from the EU FET programme (A-LEAF 732840) and from the Ministerio de Ciencia, Innovación y Universidades of Spain (project ENE2017-85087-C3-1-R).

## References

- S. Anantharaj and S. Noda, *Small*, 2020, **16**, 1905779.
- D. Huang, S. Chen, G. Zeng, X. Gong, C. Zhou, M. Cheng, W. Xue, X. Yan and J. Li, *Coord. Chem. Rev.*, 2019, **385**, 44–80.
- T. W. Kim and K.-S. Choi, *Science*, 2014, 1245026.
- J. Su, L. Guo, N. Bao and C. A. Grimes, *Nano Lett.*, 2011, **11**, 1928–1933.
- K. Sivula, F. Le Formal and M. Grätzel, *ChemSusChem*, 2011, **4**, 432–449.
- I. Cesar, A. Kay, J. A. Gonzalez Martinez and M. Grätzel, *J. Am. Chem. Soc.*, 2006, **128**, 4582–4583.
- S. U. Khan, M. Al-Shahry and W. B. Ingler, *science*, 2002, **297**, 2243–2245.
- M. Ni, M. K. Leung, D. Y. Leung and K. Sumathy, *Renewable Sustainable Energy Rev.*, 2007, **11**, 401–425.
- F. Wang, C. Di Valentin and G. Pacchioni, *J. Phys. Chem. C*, 2012, **116**, 8901–8909.
- V. Cristino, S. Caramori, R. Argazzi, L. Meda, G. L. Marra and C. A. Bignozzi, *Langmuir*, 2011, **27**, 7276–7284.
- R. Abe, M. Higashi and K. Domen, *J. Am. Chem. Soc.*, 2010, **132**, 11828–11829.
- M. Higashi, K. Domen and R. Abe, *J. Am. Chem. Soc.*, 2012, **134**, 6968–6971.
- M. Volokh, G. Peng, J. Barrio and M. Shalom, *Angew. Chem., Int. Ed.*, 2019, **58**, 6138–6151.
- S. J. Hong, S. Lee, J. S. Jang and J. S. Lee, *Energy Environ. Sci.*, 2011, **4**, 1781–1787.





- 15 S.-T. Bae, H. Shin, J. Y. Kim, H. S. Jung and K. S. Hong, *J. Phys. Chem. C*, 2008, **112**, 9937–9942.
- 16 T. W. Hamann, *Dalton Trans.*, 2012, **41**, 7830–7834.
- 17 S. Wang, P. Chen, J. H. Yun, Y. Hu and L. Wang, *Angew. Chem., Int. Ed.*, 2017, **56**, 8500–8504.
- 18 Y. Zhang, Y. Guo, H. Duan, H. Li, C. Sun and H. Liu, *Phys. Chem. Chem. Phys.*, 2014, **16**, 24519–24526.
- 19 C. Künneth, R. Batra, G. A. Rossetti Jr, R. Ramprasad and A. Kersch, in *Ferroelectricity in Doped Hafnium Oxide: Materials, Properties and Devices*, Elsevier, 2019, pp. 245–289.
- 20 S. Švarcová, K. Wiik, J. Tolchard, H. J. Bouwmeester and T. Grande, *Solid State Ionics*, 2008, **178**, 1787–1791.
- 21 M. Batzill, E. H. Morales and U. Diebold, *Phys. Rev. Lett.*, 2006, **96**, 026103.
- 22 B. M. Rajbongshi, A. Ramchiary and S. Samdarshi, *Mater. Lett.*, 2014, **134**, 111–114.
- 23 L. Liu, Z. Mei, A. Tang, A. Azarov, A. Kuznetsov, Q.-K. Xue and X. Du, *Phys. Rev. B*, 2016, **93**, 235305.
- 24 X. Pan, M.-Q. Yang, X. Fu, N. Zhang and Y.-J. Xu, *Nanoscale*, 2013, **5**, 3601–3614.
- 25 T.-Y. Yang, H.-Y. Kang, U. Sim, Y.-J. Lee, J.-H. Lee, B. Koo, K. T. Nam and Y.-C. Joo, *Phys. Chem. Chem. Phys.*, 2013, **15**, 2117–2124.
- 26 M. García-Tecedor, D. Maestre, A. Cremades and J. Piqueras, *J. Phys. D: Appl. Phys.*, 2017, **50**, 415104.
- 27 S. Carretin, Y. Hao, V. Aguilar-Guerrero, B. C. Gates, S. Trasobares, J. J. Calvino and A. Corma, *Chem. - Eur. J.*, 2007, **13**, 7771–7779.
- 28 G. Pacchioni, *ChemPhysChem*, 2003, **4**, 1041–1047.
- 29 A. Sarkar and G. G. Khan, *Nanoscale*, 2019, **11**, 3414–3444.
- 30 K. Yoshida, T. Kawai, T. Nambara, S. Tanemura, K. Saitoh and N. Tanaka, *Nanotechnology*, 2006, **17**, 3944.
- 31 U. Diebold, *Surf. Sci. Rep.*, 2003, **48**, 53–229.
- 32 M. García-Tecedor, J. Bartolomé, D. Maestre, A. Trampert and A. Cremades, *Nano Res.*, 2019, **12**, 441–448.
- 33 M. W. Gaultois and A. P. Grosvenor, *J. Mater. Chem.*, 2011, **21**, 1829–1836.
- 34 Q. Wu, Q. Zheng and R. van de Krol, *J. Phys. Chem. C*, 2012, **116**, 7219–7226.
- 35 D. Li, H. Haneda, N. K. Labhsetwar, S. Hishita and N. Ohashi, *Chem. Phys. Lett.*, 2005, **401**, 579–584.
- 36 J.-M. Wu, Y. Chen, L. Pan, P. Wang, Y. Cui, D. Kong, L. Wang, X. Zhang and J.-J. Zou, *Appl. Catal., B*, 2018, **221**, 187–195.
- 37 B. Choudhury and A. Choudhury, *J. Lumin.*, 2012, **132**, 178–184.
- 38 T. W. Kim, Y. Ping, G. A. Galli and K.-S. Choi, *Nat. Commun.*, 2015, **6**, 1–10.
- 39 Q. Liu, D. Ding, C. Ning and X. Wang, *Int. J. Hydrogen Energy*, 2015, **40**, 2107–2114.
- 40 W. Li, J. Li, X. Wang and Q. Chen, *Appl. Surf. Sci.*, 2012, **263**, 157–162.
- 41 G. Wang, Y. Ling, X. Lu, F. Qian, Y. Tong, J. Z. Zhang, V. Lordi, C. Rocha Leao and Y. Li, *J. Phys. Chem. C*, 2013, **117**, 10957–10964.
- 42 R. Van de Krol and M. Grätzel, *Photoelectrochemical Hydrogen Production*, Springer, 2012.
- 43 D.-D. Qin, T. Wang, Y.-M. Song and C.-L. Tao, *Dalton Trans.*, 2014, **43**, 7691–7694.
- 44 X. Chen, L. Liu and F. Huang, *Chem. Soc. Rev.*, 2015, **44**, 1861–1885.
- 45 M. Sachs, J.-S. Park, E. Pastor, A. Kafizas, A. A. Wilson, L. Francàs, S. Gul, M. Ling, C. Blackman and J. Yano, *Chem. Sci.*, 2019, **10**, 5667–5677.
- 46 Y. K. Kho, W. Y. Teoh, A. Iwase, L. Mädler, A. Kudo and R. Amal, *ACS Appl. Mater. Interfaces*, 2011, **3**, 1997–2004.
- 47 L. Zhou, W. Wang, L. Zhang, H. Xu and W. Zhu, *J. Phys. Chem. C*, 2007, **111**, 13659–13664.
- 48 S. Giménez and J. Bisquert, *Photoelectrochemical Solar Fuel Production*, Springer, 2016.
- 49 J. Li and N. Wu, *Catal. Sci. Technol.*, 2015, **5**, 1360–1384.
- 50 S. P. Berglund, D. W. Flaherty, N. T. Hahn, A. J. Bard and C. B. Mullins, *J. Phys. Chem. C*, 2011, **115**, 3794–3802.
- 51 Z.-F. Huang, L. Pan, J.-J. Zou, X. Zhang and L. Wang, *Nanoscale*, 2014, **6**, 14044–14063.
- 52 S. K. Pilli, T. E. Furtak, L. D. Brown, T. G. Deutsch, J. A. Turner and A. M. Herring, *Energy Environ. Sci.*, 2011, **4**, 5028–5034.
- 53 W. Luo, Z. Yang, Z. Li, J. Zhang, J. Liu, Z. Zhao, Z. Wang, S. Yan, T. Yu and Z. Zou, *Energy Environ. Sci.*, 2011, **4**, 4046–4051.
- 54 S. Selim, L. Francas, M. García-Tecedor, S. Corby, C. Blackman, S. Gimenez, J. R. Durrant and A. Kafizas, *Chem. Sci.*, 2019, **10**, 2643–2652.
- 55 D. K. Lee and K.-S. Choi, *Nat. Energy*, 2018, **3**, 53–60.
- 56 D. Cardenas-Morcoso, R. Ifraimov, M. García-Tecedor, I. Liberman, S. Gimenez and I. Hod, *J. Mater. Chem. A*, 2019, **7**, 11143–11149.
- 57 D. Kong, J. Qi, D. Liu, X. Zhang, L. Pan and J. Zou, *Trans. Tianjin Univ.*, 2019, **25**, 340–347.
- 58 Q. Pan, K. Yang, G. Wang, D. Li, J. Sun, B. Yang, Z. Zou, W. Hu, K. Wen and H. Yang, *Chem. Eng. J.*, 2019, **372**, 399–407.
- 59 S. Wang, P. Chen, Y. Bai, J. H. Yun, G. Liu and L. Wang, *Adv. Mater.*, 2018, **30**, 1800486.
- 60 Y. Chen, M. Yang, J. Du, G. Ke, X. Zhong, Y. Zhou, F. Dong, L. Bian and H. He, *J. Mater. Sci.*, 2019, **54**, 671–682.
- 61 W. Qiu, S. Xiao, J. Ke, Z. Wang, S. Tang, K. Zhang, W. Qian, Y. Huang, D. Huang and Y. Tong, *Angew. Chem.*, 2019, **131**, 19263–19271.
- 62 N. Daelman, F. S. Hegner, M. Rellán-Piñeiro, M. Capdevila-Cortada, R. García-Muelas and N. López, *J. Chem. Phys.*, 2020, **152**, 050901.
- 63 X. Xu, Y. Xu, F. Xu, G. Jiang, J. Jian, H. Yu, E. Zhang, D. Shchukin, S. Kaskel and H. Wang, *J. Mater. Chem. A*, 2020, **8**(4), 1636–1645.
- 64 W. Wang, P. J. Strohbeen, D. Lee, C. Zhou, J. K. Kawasaki, K.-S. Choi, M. Liu and G. Galli, *Chem. Mater.*, 2020, **32**, 2899–2909.
- 65 J. K. Cooper, S. B. Scott, Y. Ling, J. Yang, S. Hao, Y. Li, F. M. Toma, M. Stutzmann, K. Lakshmi and I. D. Sharp, *Chem. Mater.*, 2016, **28**, 5761–5771.



- 66 X. Yang, A. J. Fernández-Carrión, J. Wang, F. Porcher, F. Fayon, M. Allix and X. Kuang, *Nat. Commun.*, 2018, **9**, 1–11.
- 67 F. S. Hegner, D. Forrer, J. R. Galán-Mascarós, N. López and A. Selloni, *J. Phys. Chem. Lett.*, 2019, **10**, 6672–6678.
- 68 S. Selim, E. Pastor, M. García-Tecedor, M. R. Morris, L. Francas, M. Sachs, B. Moss, S. Corby, C. A. Mesa and S. Gimenez, *J. Am. Chem. Soc.*, 2019, **141**, 18791–18798.
- 69 S. Feng, T. Wang, B. Liu, C. Hu, L. Li, Z. J. Zhao and J. Gong, *Angew. Chem., Int. Ed.*, 2020, **59**, 2044–2048.
- 70 B. Zhang, L. Wang, Y. Zhang, Y. Ding and Y. Bi, *Angew. Chem., Int. Ed.*, 2018, **57**, 2248–2252.
- 71 S. Zhu, L.-a. Huang, Z. He, K. Wang, J. Guo, S.-e. Pei, H. Shao and J. Wang, *J. Electroanal. Chem.*, 2018, **827**, 42–50.
- 72 M. Grätzel, *Nature*, 2001, **414**, 338–344.
- 73 Y. Lin, S. Zhou, S. W. Sheehan and D. Wang, *J. Am. Chem. Soc.*, 2011, **133**, 2398–2401.
- 74 B. Klahr, S. Gimenez, F. Fabregat-Santiago, T. Hamann and J. Bisquert, *J. Am. Chem. Soc.*, 2012, **134**, 4294–4302.
- 75 A. Murphy, P. Barnes, L. Randeniya, I. Plumb, I. Grey, M. Horne and J. Glasscock, *Int. J. Hydrogen Energy*, 2006, **31**, 1999–2017.
- 76 K. Sivula, R. Zboril, F. Le Formal, R. Robert, A. Weidenkaff, J. Tucek, J. Frydrych and M. Gratzel, *J. Am. Chem. Soc.*, 2010, **132**, 7436–7444.
- 77 M. P. Dare-Edwards, J. B. Goodenough, A. Hamnett and P. R. Trevellick, *J. Chem. Soc., Faraday Trans. 1*, 1983, **79**, 2027–2041.
- 78 M. G. Walter, E. L. Warren, J. R. McKone, S. W. Boettcher, Q. Mi, E. A. Santori and N. S. Lewis, *Chem. Rev.*, 2010, **110**, 6446–6473.
- 79 I. Cesar, K. Sivula, A. Kay, R. Zboril and M. Grätzel, *J. Phys. Chem. C*, 2009, **113**, 772–782.
- 80 Y. Ling, G. Wang, D. A. Wheeler, J. Z. Zhang and Y. Li, *Nano Lett.*, 2011, **11**, 2119–2125.
- 81 D. A. Wheeler, G. Wang, Y. Ling, Y. Li and J. Z. Zhang, *Energy Environ. Sci.*, 2012, **5**, 6682–6702.
- 82 S. D. Tilley, M. Cornuz, K. Sivula and M. Grätzel, *Angew. Chem., Int. Ed.*, 2010, **49**, 6405–6408.
- 83 B. Klahr, S. Gimenez, F. Fabregat-Santiago, J. Bisquert and T. W. Hamann, *J. Am. Chem. Soc.*, 2012, **134**, 16693–16700.
- 84 S. Shen, S. A. Lindley, X. Chen and J. Z. Zhang, *Energy Environ. Sci.*, 2016, **9**, 2744–2775.
- 85 Y. Ling, G. Wang, J. Reddy, C. Wang, J. Z. Zhang and Y. Li, *Angew. Chem., Int. Ed.*, 2012, **51**, 4074–4079.
- 86 M. Zhang, W. Luo, Z. Li, T. Yu and Z. Zou, *Appl. Phys. Lett.*, 2010, **97**, 042105.
- 87 A. Pu, J. Deng, M. Li, J. Gao, H. Zhang, Y. Hao, J. Zhong and X. Sun, *J. Mater. Chem. A*, 2014, **2**, 2491–2497.
- 88 L. Steier, I. Herráiz-Cardona, S. Gimenez, F. Fabregat-Santiago, J. Bisquert, S. D. Tilley and M. Grätzel, *Adv. Funct. Mater.*, 2014, **24**, 7681–7688.
- 89 Y. Makimizu, N. T. Nguyen, J. Tucek, H. J. Ahn, J. Yoo, M. Poornajar, I. Hwang, S. Kment and P. Schmuki, *Chem. - Eur. J.*, 2020, **26**, 2685–2692.
- 90 X. Zhang, P. Klaver, R. van Santen, M. Van De Sanden and A. Bieberle-Hütter, *J. Phys. Chem. C*, 2016, **120**, 18201–18208.
- 91 M.-T. Nguyen, S. Piccinin, N. Seriani and R. Gebauer, *ACS Catal.*, 2015, **5**, 715–721.
- 92 A. Hellman, B. Iandolo, B. Wickman, H. Grönbeck and J. Baltrusaitis, *Surf. Sci.*, 2015, **640**, 45–49.
- 93 J. Hu, X. Zhao, W. Chen and Z. Chen, *ACS Omega*, 2018, **3**, 14973–14980.
- 94 Q. Yang, J. Du, J. Li, Y. Wu, Y. Zhou, Y. Yang, D. Yang and H. He, *ACS Appl. Mater. Interfaces*, 2020, **12**, 11625–11634.
- 95 A. Fujishima and K. Honda, *Nature*, 1972, **238**, 37–38.
- 96 X. Chen and S. S. Mao, *Chem. Rev.*, 2007, **107**, 2891–2959.
- 97 F. Fresno, R. Portela, S. Suárez and J. M. Coronado, *J. Mater. Chem. A*, 2014, **2**, 2863–2884.
- 98 A. J. Haider, R. H. AL-Anbari, G. R. Kadhim and C. T. Salame, *Energy Procedia*, 2017, **119**, 332–345.
- 99 J. Zhang, P. Zhou, J. Liu and J. Yu, *Phys. Chem. Chem. Phys.*, 2014, **16**, 20382–20386.
- 100 R. Zallen and M. Moret, *Solid State Commun.*, 2006, **137**, 154–157.
- 101 D. A. Hanaor and C. C. Sorrell, *J. Mater. Sci.*, 2011, **46**, 855–874.
- 102 A. L. Linsebigler, G. Lu and J. T. Yates Jr, *Chem. Rev.*, 1995, **95**, 735–758.
- 103 C. Byrne, G. Subramanian and S. C. Pillai, *J. Environ. Chem. Eng.*, 2018, **6**, 3531–3555.
- 104 W. J. Youngblood, S.-H. A. Lee, Y. Kobayashi, E. A. Hernandez-Pagan, P. G. Hoertz, T. A. Moore, A. L. Moore, D. Gust and T. E. Mallouk, *J. Am. Chem. Soc.*, 2009, **131**, 926–927.
- 105 X.-F. Gao, H.-B. Li, W.-T. Sun, Q. Chen, F.-Q. Tang and L.-M. Peng, *J. Phys. Chem. C*, 2009, **113**, 7531–7535.
- 106 R. Asahi, T. Morikawa, H. Irie and T. Ohwaki, *Chem. Rev.*, 2014, **114**, 9824–9852.
- 107 J. H. Park, S. Kim and A. J. Bard, *Nano Lett.*, 2006, **6**, 24–28.
- 108 X. Chen and C. Burda, *J. Am. Chem. Soc.*, 2008, **130**, 5018–5019.
- 109 J. Yan, H. Wu, H. Chen, Y. Zhang, F. Zhang and S. F. Liu, *Appl. Catal., B*, 2016, **191**, 130–137.
- 110 H. M. El-Bery, Y. Matsushita and A. Abdel-moneim, *Appl. Surf. Sci.*, 2017, **423**, 185–196.
- 111 C. Hao, W. Wang, R. Zhang, B. Zou and H. Shi, *Sol. Energy Mater. Sol. Cells*, 2018, **174**, 132–139.
- 112 H. Liu, H. Ma, X. Li, W. Li, M. Wu and X. Bao, *Chemosphere*, 2003, **50**, 39–46.
- 113 V. E. Henrich and P. A. Cox, *The Surface Science of Metal Oxides*, Cambridge University Press, 1996.
- 114 J. Nowotny, T. Bak, M. Nowotny and L. Sheppard, *J. Phys. Chem. B*, 2006, **110**, 18492–18495.
- 115 G. Vásquez, S. Z. Karazhanov, D. Maestre, A. Cremades, J. Piqueras and S. E. Foss, *Phys. Rev. B*, 2016, **94**, 235209.
- 116 T. Berger, M. Sterrer, O. Diwald, E. Knözinger, D. Panayotov, T. L. Thompson and J. T. Yates, *J. Phys. Chem. B*, 2005, **109**, 6061–6068.
- 117 D. Cronmeyer, *Phys. Rev.*, 1959, **113**, 1222.



- 118 G. Wang, H. Wang, Y. Ling, Y. Tang, X. Yang, R. C. Fitzmorris, C. Wang, J. Z. Zhang and Y. Li, *Nano Lett.*, 2011, **11**, 3026–3033.
- 119 H. Cui, W. Zhao, C. Yang, H. Yin, T. Lin, Y. Shan, Y. Xie, H. Gu and F. Huang, *J. Mater. Chem. A*, 2014, **2**, 8612–8616.
- 120 G. Li, Z. Lian, X. Li, Y. Xu, W. Wang, D. Zhang, F. Tian and H. Li, *J. Mater. Chem. A*, 2015, **3**, 3748–3756.
- 121 Q. Kang, J. Cao, Y. Zhang, L. Liu, H. Xu and J. Ye, *J. Mater. Chem. A*, 2013, **1**, 5766–5774.
- 122 T. Xia, Y. Zhang, J. Murowchick and X. Chen, *Catal. Today*, 2014, **225**, 2–9.
- 123 M. N. Shaddad, D. Cardenas-Morcoso, M. García-Tecedor, F. Fabregat-Santiago, J. Bisquert, A. M. Al-Mayouf and S. Gimenez, *ACS Omega*, 2019, **4**(14), 16095–16102.
- 124 T. L. Thompson and J. T. Yates, *Chem. Rev.*, 2006, **106**, 4428–4453.
- 125 T.-C. Lu, S.-Y. Wu, L.-B. Lin and W.-C. Zheng, *Phys. B*, 2001, **304**, 147–151.
- 126 X. Chen, L. Liu, Y. Y. Peter and S. S. Mao, *Science*, 2011, **331**, 746–750.
- 127 J. Tang, A. J. Cowan, J. R. Durrant and D. R. Klug, *J. Phys. Chem. C*, 2011, **115**, 3143–3150.
- 128 F. M. Pesci, G. Wang, D. R. Klug, Y. Li and A. J. Cowan, *J. Phys. Chem. C*, 2013, **117**, 25837–25844.
- 129 H. Song, C. Li, Z. Lou, Z. Ye and L. Zhu, *ACS Sustainable Chem. Eng.*, 2017, **5**, 8982–8987.
- 130 S. Li, J. Qiu, M. Ling, F. Peng, B. Wood and S. Zhang, *ACS Appl. Mater. Interfaces*, 2013, **5**, 11129–11135.
- 131 L. Hou, M. Zhang, Z. Guan, Q. Li and J. Yang, *Appl. Surf. Sci.*, 2018, **428**, 640–647.
- 132 K. Zhang, S. Ravishankar, M. Ma, G. Veerappan, J. Bisquert, F. Fabregat-Santiago and J. H. Park, *Adv. Energy Mater.*, 2017, **7**, 1600923.
- 133 X. Liu, F. Wang and Q. Wang, *Phys. Chem. Chem. Phys.*, 2012, **14**, 7894–7911.
- 134 G. Liu, J. Han, X. Zhou, L. Huang, F. Zhang, X. Wang, C. Ding, X. Zheng, H. Han and C. Li, *J. Catal.*, 2013, **307**, 148–152.
- 135 S. Sfaelou, L.-C. Pop, O. Monfort, V. Dracopoulos and P. Lianos, *Int. J. Hydrogen Energy*, 2016, **41**, 5902–5907.
- 136 Q. Mi, A. Zhanaidarova, B. S. Bruntschwig, H. B. Gray and N. S. Lewis, *Energy Environ. Sci.*, 2012, **5**, 5694–5700.
- 137 Y.-H. Chew, J.-Y. Tang, L.-J. Tan, B. W. J. Choi, L.-L. Tan and S.-P. Chai, *Chem. Commun.*, 2019, **55**, 6265–6268.
- 138 S. S. Kalanur, J.-Y. Hwang and H. Seo, *J. Catal.*, 2017, **350**, 197–202.
- 139 Y. Bu, Z. Chen and C. Sun, *Appl. Catal., B*, 2015, **179**, 363–371.
- 140 J. Cao, B. Luo, H. Lin, B. Xu and S. Chen, *Appl. Catal., B*, 2012, **111**, 288–296.
- 141 M. Gillet, C. Lemire, E. Gillet and K. Aguir, *Surf. Sci.*, 2003, **532**, 519–525.
- 142 M. Gerosa, F. Gygi, M. Govoni and G. Galli, *Nat. Mater.*, 2018, **17**, 1122–1127.
- 143 E. Albanese, C. Di Valentin and G. Pacchioni, *ACS Appl. Mater. Interfaces*, 2017, **9**, 23212–23221.
- 144 T. Singh, R. Müller, J. Singh and S. Mathur, *Appl. Surf. Sci.*, 2015, **347**, 448–453.
- 145 S. A. Ansari, M. M. Khan, S. Kalathil, A. Nisar, J. Lee and M. H. Cho, *Nanoscale*, 2013, **5**, 9238–9246.
- 146 J. Zhang, X. Chang, C. Li, A. Li, S. Liu, T. Wang and J. Gong, *J. Mater. Chem. A*, 2018, **6**, 3350–3354.
- 147 T. Soltani, A. Tayyebi, H. Hong, M. H. Mirfasih and B.-K. Lee, *Sol. Energy Mater. Sol. Cells*, 2019, **191**, 39–49.
- 148 J. Cen, Q. Wu, D. Yan, W. Zhang, Y. Zhao, X. Tong, M. Liu and A. Orlov, *RSC Adv.*, 2019, **9**, 899–905.
- 149 S. Corby, L. Francàs, A. Kafizas and J. R. Durrant, *Chem. Sci.*, 2020, **11**, 2907–2914.
- 150 M. Yang, H. He, J. Du, H. Peng, G. Ke and Y. Zhou, *J. Phys. Chem. Lett.*, 2019, **10**, 6159–6165.

